Atmos. Chem. Phys., 26, 6223–6241, 2026
https://doi.org/10.5194/acp-26-6223-2026

Atmospheric Chemistry and Physics
Open Access
EGU

Research article

The role of chemical boundary conditions in simulating summer ozone and cross-boundary transport over China

Yunsong Du[1,2], Fumo Yang[1], Sijia Lou[3], Baolei Lyu[4], Ran Huang[5], Guangming Shi[1], Yongtao Hu[6], Yan Jiang[7], and Nan Wang[1]

[1]College of carbon Neutrality Future Technology, Sichuan University, Chengdu 610065, China
[2]Department of Environmental Science and Engineering, Sichuan University, Chengdu 610065, China
[3]School of Atmospheric Sciences, Nanjing University, Nanjing 210023, China
[4]Huayun Sounding Meteorological Technology Co. Ltd., Beijing 100081, China
[5]Hangzhou AiMa Technologies, Hangzhou, Zhejiang 311121, China
[6]School of Civil and Environmental Engineering, Georgia Institute of Technology, Atlanta, Georgia 30332, USA
[7]Sichuan Eco-environment Monitoring Station, Chengdu 610091, China

Correspondence: Nan Wang (nan.wang@scu.edu.cn)

Received: 24 October 2025 – Discussion started: 11 January 2026
Revised: 13 April 2026 – Accepted: 23 April 2026 – Published: 11 May 2026

Abstract. Regional chemical transport models are vital for diagnosing and forecasting tropospheric ozone (O_3) pollution. However, their accuracy is often limited by the simplified treatment of chemical boundary condition (CBC). This study provides a comprehensive evaluation of how different CBC influence regional O_3 simulations over China using the WRF–CMAQ model. Four CBC scenarios were assessed: a static BASE profile representing climatological conditions and three dynamic scenarios derived from H-CMAQ, GEOS-Chem, and CESM2.2. Model results were validated with surface networks, ozonesonde profiles, and satellite O_3 columns. The BASE scenario underestimated the average maximum daily 8 h O_3 (avg-O3MDA8) and its 90th percentile by −5.7 % and −13.1 %, respectively, while dynamic CBC substantially improved the accuracy. GEOS-Chem achieved the lowest bias (−0.3 %) and highest agreement (IOA = 0.85 and 0.83) for avg-O3MDA8 and its 90th percentile. H-CMAQ performed best in high-elevation northwestern regions, and CESM2.2 excelled in southern and southwestern areas. Vertically, all CBC reasonably matched observations within the troposphere, but elevated lower-stratosphere biases were identified in BASE, H-CMAQ, and CESM2.2. A case study contrasting cyclone-scavenging and post-trough accumulation phases revealed that dynamic CBC enhance cross-boundary transport efficiency, raising O_3 by 10 %–20 % over eastern China through combined continental and stratospheric inflows. These results underscore the crucial role of synoptic circulation-driven transboundary transport in shaping regional O_3 concentrations and demonstrate the importance of realistic, time-varying CBC for improving regional O_3 simulations, air quality forecasting, and transboundary pollution management in China.

Key points.

- We systematically evaluated the impacts of chemical boundary conditions (static vs. dynamic) on regional O_3 simulations over China.
- Chemical boundary conditions strongly modulate O_3 simulations via cross-boundary transport in both horizontal and vertical directions.
- Synoptic circulation dynamically amplifies the impacts of chemical boundary conditions on regional O_3 levels.

Published by Copernicus Publications on behalf of the European Geosciences Union.

1 Introduction

Ozone (O_3) pollution is a critical environmental issue with profound implications for air quality (Malley et al., 2017; Chiu et al., 2023). As a secondary pollutant, tropospheric O_3 is mainly formed through photochemical reactions involving precursors such as nitrogen oxides (NO_x) and volatile organic compounds (VOCs) under sunlight. Elevated O_3 concentrations pose severe risks to public health, contributing to respiratory diseases and premature mortality, while also damaging ecosystems and suppressing agricultural productivity (WHO, 2016; Wang et al., 2017; Zhang et al., 2019a). In addition, as a highly reactive oxidant, tropospheric O_3 regulates the atmospheric lifetime of numerous reactive trace gases by governing their chemical transformations (Jacob, 2003).

O_3 pollution is currently one of the most pressing environmental challenges faced globally. In many Western countries, stringent air pollution controls implemented since the last century have led to stabilization or even declines in O_3 concentrations (Monks et al., 2015; Tarasick et al., 2019). Over the past decades, China has experienced frequent high-ozone episodes, drawing increasing attention from both the scientific community and policymakers. Even though, China has only more recently undertaken aggressive air quality improvement measures, most notably through the Air Pollution Prevention and Control Action Plan launched in 2012, which mandated substantial reductions in nitrogen oxide emissions. Despite these efforts, O_3 concentrations in China have not shown a sustained decline; instead, they have continued to rise in major urban agglomerations such as the North China Plain and the Yangtze River Delta (Zhang et al., 2019b; Lu et al., 2020; Wang et al., 2020, 2022). Nevertheless, the formation and distribution of O_3 are governed by the interplay of precursor emissions, meteorology, and transport processes. Variations in the magnitude and composition of anthropogenic and natural NO_x and VOC emissions shape the chemical regime for O_3 production and loss. Meteorological conditions (e.g., temperature, solar radiation, humidity, boundary layer dynamics, and circulation patterns) further modulate photochemical reaction rates, vertical mixing, and horizontal transport, while surface characteristics and complex topography can influence local stagnation and recirculation. Together with regional and transboundary transport, as well as inflow from the free troposphere and occasional stratosphere–troposphere exchange, these processes determine background O_3 levels and lead to strong spatial and seasonal heterogeneity in O_3 pollution (Monks et al., 2015; Lu et al., 2018). Regional chemical transport models (CTMs) are essential tools for predicting and diagnosing air pollution, particularly photochemical O_3 pollution. Unlike global models, which emphasize large-scale atmospheric processes at coarse spatial resolutions, regional models such as the Community Multiscale Air Quality (CMAQ) and the Weather Research and Forecasting model with Chemistry (WRF-Chem) resolve chemical and physical processes at finer spatial and temporal scales (Byun and Schere, 2006; Grell et al., 2005). This capability enables them to capture the complex interactions among local emissions, meteorology, and topography that govern the formation, transport, and dispersion of O_3 and its precursors. However, the reliability of CTM-based O_3 simulations ultimately depends on the accuracy and consistency of the meteorological fields, emission inputs, and chemical boundary conditions that define the model environment (Hogrefe et al., 2018; Solazzo et al., 2012).

Over the past decade, CTMs have become central to air quality forecasting, scientific research, environmental assessment and policy evaluation (Yahya et al., 2015; Bai et al., 2018; Wang et al., 2021b; Gao et al., 2024). Their flexible domain configurations allow targeted simulations over regions with intense emissions or complex terrain, such as urban agglomerations and mountainous areas (Wang et al., 2019; Mao et al., 2022a; Dou et al., 2024). Besides, incorporating high-resolution emission inventories and region-specific meteorological inputs further enhances their accuracy. Numerous applications have demonstrated their scientific and practical value: Zhang et al. (2019b) used WRF-CMAQ to disentangle the relative roles of anthropogenic emissions and meteorology in $PM_{2.5}$ variability, while Mao et al. (2022a) reproduced multi-pollutant trends across China between 2013 and 2019, validating CMAQ's long-term performance. Wang et al. (2024) applied CMAQ to assess regional O_3 responses during heatwaves, highlighting the strong sensitivity of O_3 formation to both emissions and meteorological drivers. Collectively, these applications underscore the indispensable role of regional CTMs in advancing mechanistic understanding of air pollution and in guiding effective clean-air strategies (Yahya et al., 2015; Lei et al., 2023; Dou et al., 2024; Geng et al., 2024).

Building on this foundation, substantial efforts have focused on improving the performance and reliability of regional CTMs. A major area of optimization lies in chemical mechanisms: updated frameworks such as Carbon Bond 6 (CB6) and SAPRC-11 enhance model fidelity in representing O_3 formation pathways and secondary organic aerosol production under diverse atmospheric conditions (Yarwood et al., 2010; Carter and Heo, 2013). Parallel improvements in meteorological simulations – through techniques such as four-dimensional data assimilation (FDDA) in WRF and the incorporation of high-resolution land-use datasets (e.g., MODIS, NLCD) – have sharpened the representation of surface temperature, planetary boundary layer height, and wind fields (Mallard et al., 2018; Campbell et al., 2019; Godowitch et al., 2015; Wang et al., 2021a; Siewert and Kroszczynski, 2023). Meanwhile, advances in anthropogenic and biogenic emission inventories, including the Multi-resolution Emission Inventory for China (MEIC) and the U.S. National Emissions Inventory (NEI), now provide finer spatial and temporal detail, capturing sector-specific variability and reducing input uncertainty (Li et al., 2017a; Zheng et al., 2021; Foley et al., 2023; Geng et al., 2024). Together, these contin-

uous advancements have considerably strengthened the capacity of regional CTMs to support both scientific inquiry and evidence-based policy-making.

Despite substantial advances in regional chemical transport models (CTMs), comparatively little attention has been devoted to chemical boundary conditions (CBC), even though they critically influence model accuracy. CBC specify the concentrations of air pollutants at the lateral and vertical boundaries of the simulation domain, thereby constraining internal chemical evolution and pollutant transport (Goldberg et al., 2015; Hogrefe et al., 2018). Accurate CBC are essential for capturing the impact of long-range pollutant transport and representing background concentrations, both of which strongly shape regional air quality. For regional O_3, these boundary-driven background levels can modulate the effectiveness of local emission controls, alter the chemical sensitivity regime, and partly determine the spatial gradients between upwind and downwind areas. In regions strongly influenced by continental outflow, stratosphere–troposphere exchange, or marine inflow, poorly specified CBC may therefore lead to systematic biases in simulated O_3 distributions (Zhu et al., 2024; Goldberg et al., 2015; Hogrefe et al., 2018). Oversimplified treatments – such as prescribing fixed background values or climatological means – can introduce substantial biases, resulting in misrepresentation of pollutant levels and misleading evaluations of source contributions, policy effectiveness, and health risks (Yahya et al., 2015; Hogrefe et al., 2018). Indeed, sensitivity studies show that uncertainties in CBC can alter simulated O_3 by several parts per billion, with particularly pronounced effects in downwind and coastal regions influenced by transboundary transport (Hogrefe et al., 2018; Jerrett et al., 2005).

In China, few studies have systematically assessed the role of chemical boundary conditions in influencing model performance or pollutant attribution across different geographical regions (Zhu et al., 2024). This represents a critical gap, as the spatial heterogeneity of transboundary influences – from continental transport in the west to marine outflow in the east – could lead to regionally differentiated impacts on pollutant concentrations and control policy outcomes. For example, western and northern China may be more strongly affected by inflow of polluted air masses from upwind continental source regions, while eastern coastal areas can be influenced by recirculation and clean or polluted marine air, leading to distinct baseline O_3 levels and vertical structures. Without an explicit assessment of CBC across these contrasting regimes, regional CTM applications may under- or overestimate O_3 burdens and misattribute observed spatial patterns to local emissions or meteorology alone (Solazzo et al., 2012; Ni et al., 2018; Sahu et al., 2021; Mao et al., 2022b; Shen et al., 2024). Therefore, a comprehensive evaluation of the role of chemical boundary conditions in regional CTM applications is urgently needed to enhance model reliability, reduce forecast uncertainty, and support the formulation of more effective O_3 mitigation strategies.

Herein, we used outputs from three global chemical transport models to provide downscaled CBC for the regional CMAQ model and systematically evaluated the impact of including versus omitting CBC on O_3 simulations. Surface observations, ozonesonde profiles, and satellite data were used to assess model performance across China. We also examine the mechanisms by which CBC influence O_3, including their regulation of background concentrations and propagation of transboundary pollutants into the domain. This study advances understanding of CBC in regional air quality modeling and provides a foundation for more accurate high-resolution O_3 forecasts and improved air quality management strategies. By explicitly contrasting simulations with and without chemically consistent CBC, while keeping emissions and meteorology unchanged, this study isolates the contribution of boundary conditions from other key drivers of O_3 variability. The resulting diagnostics provide a clearer physical interpretation of how CBC interact with regional emissions and meteorological fields to shape O_3 distributions over China.

2 Data and Method

2.1 Modelling Configuration

In this study, O_3 concentrations during July–August 2019 were simulated using the WRF-CMAQ modeling system. The Weather Research and Forecasting (WRF, https://www.mmm.ucar.edu/models/wrf, last access: 12 April 2026) model version 3.9.1 was used to generate meteorological fields, which were then provided as inputs to drive the Community Multiscale Air Quality (CMAQ) model version 5.3.3 (http://www.epa.gov/cmaq, last access: 12 April 2026). CMAQ solves the governing physical and chemical equations to simulate the three-dimensional distribution of air pollutants. The simulations were conducted at a horizontal resolution of 36 km, covering the entire Chinese mainland and surrounding regions to ensure adequate representation of regional transport processes (see Fig. 1). The meteorological initial and boundary conditions were derived from the ERA5 reanalysis dataset ($0.25° \times 0.25°$ resolution), provided by the Copernicus Climate Change Service via the Climate Data Store (CDS) (Hersbach et al., 2023). Anthropogenic emissions over China were obtained from the Multi-resolution Emission Inventory for China (MEIC v1.4) for the year 2019 (Li et al., 2017a), which provides sector-based emissions mapped to CMAQ species (http://meicmodel.org, last access: 1 January 2024). For regions outside China, anthropogenic emissions were based on the MIX v1.1 inventory (Li et al., 2017b). This dataset provides monthly grid-based emission data at a 0.25° spatial resolution across five key sectors (power, industry, residential, transport, and agriculture), meeting the requirements for multi-scale atmospheric chemical transport modeling (http://meicmodel.org.cn, last access: 13 April 2026). The biogenic emissions were estimated using

the inline Biogenic Emission Inventory System (BEIS3) embedded within CMAQ which dynamically calculates emissions based on land use, vegetation type, and meteorological conditions online. The gas-phase chemistry was represented using the SAPRC07TC mechanism, while aerosol processes were simulated using the AERO6 module.

In order to assess the influence of CBC on O_3, four different CBC scenarios were designed and applied as inputs to the CMAQ BCON (boundary condition) module. The first scenario, referred to as BASE, employs a spatially uniform and temporally constant boundary condition derived from the built-in ASCII vertical profiles in CMAQ. These profiles were extracted from a hemispheric CMAQv5.3 beta2 simulation for the year 2016, representing annual mean concentrations at the grid cell nearest to (37° N, 157° W), which is over the ocean in the central North Pacific region. Therefore, the BASE CBC represent the background profile of the open ocean environment. In contrast, the remaining three scenarios utilize boundary conditions generated from the output of three global chemistry models (GCMs), namely, Hemisphere version of the Community Multiscale Air Quality model (H-CMAQ), Goddard Earth Observing System-Chemistry (GEOS-Chem), and Community Earth System Model version 2.2 (CESM2.2). Each of these boundary datasets was processed and formatted consistently to ensure compatibility with the CMAQ framework.

Specifically, CBC for the H-CMAQ scenario were derived from daily averaged species concentration outputs produced by a hemispheric CMAQ simulation under the U.S. EPA's Air Quality Time Series (EQUATES) Project (https://www.epa.gov/cmaq/EQUATES, last access: 4 April 2026). These simulations were conducted using a customized version of CMAQ v5.3.2, with a horizontal resolution of 108×108 km on a polar stereographic projection, and employed the CB6R3M_AE7_KMTBR chemical mechanism.

For the GEOS-Chem scenario, 3-hourly global simulation outputs were used. The GEOS-Chem model is a global 3-D chemical transport model driven by meteorological fields from NASA's Goddard Earth Observing System (GEOS), developed by the NASA Global Modeling and Assimilation Office. The chemical mechanism includes comprehensive tropospheric O_3–NO_x–VOCs–aerosol–halogen chemistry (Mao et al., 2013; Park et al., 2004; Parrella et al., 2012; Wang et al., 1998), as well as stratospheric chemistry processes (Eastham et al., 2014). Further information is available at https://geoschem.github.io/ (last access: 4 April 2026).

The CESM2.2 scenario utilized 6-hourly output from the Community Atmosphere Model with Chemistry (CAM-chem) embedded within the Community Earth System Model version 2.2 (CESM2.2). The CAM-chem simulations used the finite-volume dynamical core, with a horizontal resolution of $1° \times 1°$ and 32 vertical levels. The MOZART-T1 mechanism was applied to simulate both tropospheric and stratospheric chemical processes. Details on the model setup and outputs are available at https://www2.acom.ucar.edu/gcm/cam-chem (last access: 4 April 2026).

All three global model outputs were converted to the I/O API format required by the CMAQ Chemical Transport Model (CCTM). A combination of data transformation tools and custom scripts was developed and applied to harmonize species mapping, spatial resolution, temporal alignment, and file formatting, thus enabling seamless integration of each global model dataset as boundary conditions for the regional CMAQ simulations. To minimize the influence of initial conditions and allow the imposed boundary conditions to fully propagate throughout the simulation domain, a 10 d model spin-up period was applied prior to the analysis period.

2.2 Observation data

2.2.1 Surface observation data

Surface observations across China for July–August 2019 were used to evaluate the simulated meteorological parameters and atmospheric pollutant concentrations from the WRF-CMAQ model. Meteorological data were obtained from the National Meteorological Information Center (http://data.cma.cn, last access: 4 April 2026). Hourly meteorological observations from 2394 monitoring stations were collected, including 2 m air temperature ($T2$), 2 m relative humidity (RH2), 10 m wind speed (WS10), and surface pressure (PRS). Hourly O_3 observations were retrieved from the China National Environmental Monitoring Center (https://air.cnemc.cn:18007, last access: 4 April 2026), encompassing data from 1480 air quality monitoring sites. The spatial distribution of meteorological and air quality monitoring stations is shown in Fig. 1 and Fig. S1 in the Supplement. To investigate the spatial variability of chemical boundary condition impacts on O_3 simulation, monitoring sites were grouped into seven regions within China (Fig. 1 and Table S1): South (S), East (E), North (N), Central (C), Northeast (NE), Northwest (NW), and Southwest (SW).

This study evaluates sites O_3 using the Maximum Daily 8 h Average concentration (O3MDA8), derived from both surface observations and model simulations. To comprehensively assess model performance across different pollution levels, we analyze two key indicators: the average O3MDA8 (avg-O3MDA8), which reflects the overall background and typical exposure level, and the 90th percentile of O3MDA8 (90th-O3MDA8), which is used to characterize high-O_3 events. The inclusion of the 90th percentile metric enables evaluation of the model's ability to capture peak O_3 pollution episodes that are most relevant to regulatory thresholds and public health risk assessments.

Model performance was quantitatively evaluated using multiple statistical metrics, including mean observed value (OBS), mean simulated value (SIM) for each of the four CBC scenarios (BASE, H-CMAQ, GEOS-Chem, CESM2.2), mean bias (MB), normalized mean bias (NMB), root mean

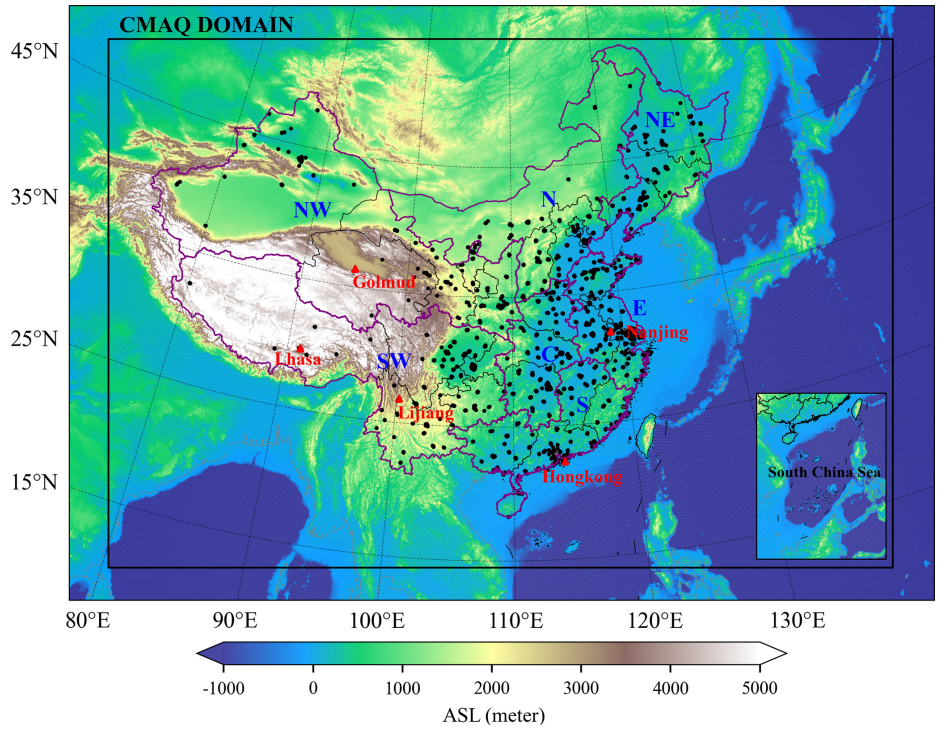

Figure 1. Simulation domain of the CMAQ model with a horizontal resolution of $36 \times 36\,km^2$. Black dots represent surface O_3 monitoring sites, and red triangles denote O_3 sounding launch stations. Terrain elevation above sea level (ASL) is illustrated with shaded relief. Purple lines delineate the administrative boundaries of China's major regions – South (S), East (E), North (N), Central (C), Northeast (NE), Northwest (NW), and Southwest (SW). The provinces included in each region are listed in Table S1.

square error (RMSE), index of agreement (IOA), and Pearson correlation coefficient (r). The IOA ranges from 0 to 1, where 1 indicates a perfect match between simulated and observed values, while values approaching 0 indicate poor model performance (Willmott, 1981). The mathematical definitions of these statistics are provided below.

$$\mathrm{OBS} = \frac{1}{n}\sum_{i=1}^{n} O_i \tag{1}$$

$$\mathrm{SIM} = \frac{1}{n}\sum_{i=1}^{n} S_i \tag{2}$$

$$\mathrm{MB} = \frac{1}{n}\sum_{i=1}^{n}(S_i - O_i) \tag{3}$$

$$\mathrm{NMB} = \sum_{i=1}^{n}(S_i - O_i)/\sum_{i=1}^{n} O_i \tag{4}$$

$$\mathrm{RMSE} = \sqrt{\frac{1}{n}\sum_{i=1}^{n}(S_i - O_i)^2} \tag{5}$$

$$r = \frac{\sum_{i=1}^{n}(S_i - \mathrm{SIM})(O_i - \mathrm{OBS})}{\sqrt{\sum_{i=1}^{n}(S_i - \mathrm{SIM})^2}\sqrt{\sum_{i=1}^{n}(O_i - \mathrm{OBS})^2}} \tag{6}$$

$$\mathrm{IOA} = 1 - \frac{n \times \mathrm{RMSE}^2}{\sum_{i=1}^{n}(|S_i - \mathrm{OBS}| + |O_i - \mathrm{OBS}|)^2} \tag{7}$$

where S_i and O_i are the simulated and observed site's avg-O3MDA8 or 90th-O3MDA8, n represents the number of the simulated days.

2.2.2 Vertical Observation Data

To evaluate the influence of CBC on the vertical distribution of O_3, O_3 sounding data from five representative sites (Hong Kong, Nanjing, Golmud, Lhasa, and Lijiang) were collected and used to validate the model's vertical O_3 simulations. These stations are strategically located in the eastern, southern, southwestern, and northwestern boundaries of the modeling domain (Fig. 1), enabling a targeted assessment of how boundary conditions affect O_3 concentrations aloft. Briefly, the Hong Kong profiles (King's Park Observatory; launched at 13:00 LST; 9 soundings during July–August 2019) were obtained from the World Ozone and Ultraviolet Radiation Data Centre (WOUDC, https://woudc.org/data.php, last access: 8 October 2024). Nanjing observations (from the National Benchmark Climate Station; launched between 13:00

and 14:00 LST; 4 soundings between 23 July 2019 and 1 September 2020) were sourced from the China Air Pollution Data Center (CAPDC, https://www.capdatabase.cn, last access: 4 April 2026). Data for Golmud (12 profiles), Lhasa (8 profiles), and Lijiang (5 profiles), collected between 2019 and 2022 with launch times ranging from 23:00 to 02:00 LST, were obtained from the National Tibetan Plateau Data Center (TPDC, https://data.tpdc.ac.cn/home, last access: 10 October 2024) (Bai, 2022; Bai and Bian, 2022a, b). To ensure consistency across datasets and comparability with the model output, all sonde data were processed for the 0–20 km height above ground level (HAGL) range and interpolated to match the model vertical structure, and data within the 0–16 km HAGL layer were used in the model evaluation. Observations during July–August were prioritized, and model outputs were extracted as time-averaged vertical profiles over the corresponding grid cells and times (13:00–14:00 or 23:00–02:00 LST). Detailed information about the surface observation and sounding sites is provided in Table S2.

In addition, tropospheric O_3 column data were also introduced to further evaluate the spatial performance of the model. This dataset was developed by the University of Science and Technology of China (USTC) and is derived from measurements by the Environmental Trace Gases Monitoring Instrument (EMI) aboard the Gaofen-5 satellite, China's first ultraviolet-visible hyperspectral spectrometer dedicated to atmospheric composition monitoring. The product provides a seamless tropospheric O_3 column dataset at a high spatial resolution of 1 km × 1 km, offering detailed information on O_3 distribution over complex terrains and urban regions. Further details on the retrieval algorithm and validation of the product can be found in Zhao et al. (2024). Detailed information about the tropospheric O_3 column data is also provided in Table S2.

3 Results and Discussions

3.1 Comparative Analysis of four CBC

Figure 2 displays the vertically averaged temporal O_3 distribution along the four lateral boundaries of the modelling domain during July–August 2019, under four different CBC scenarios. In the BASE scenario, the O_3 profile remains static, characterized by horizontally uniform mixing ratios at each altitude. A sharp increase in O_3 concentration is evident near the tropopause, with minimal vertical variation in the lower and mid-troposphere. This relatively uniform, three-dimensional O_3 distribution suggests that the BASE CBC scenario represents a background condition (i.e., over the open ocean), and thus fails to adequately capture the spatiotemporal variability of O_3 over mainland East Asia, where O_3 levels are strongly influenced by anthropogenic emissions and regional transport processes.

In contrast to the static pattern in the BASE scenario, the O_3 boundary conditions extracted from the three global models (H-CMAQ, GEOS-Chem, and CESM2.2) exhibit both horizontal and vertical variability across the four lateral boundaries. These three scenarios display a generally consistent spatial and vertical structure. However, notable differences still exist across different boundaries. In the lower troposphere (0–3 km), the average O_3 concentrations from the three global models are 5–7 ppbv lower than those in the BASE scenario along the southern and eastern boundaries, with only minor differences among the models. For instance, over the oceanic portions of these boundaries, specifically the eastern segment of the southern boundary and the southern segment of the eastern boundary, the BASE scenario overestimates boundary O_3 concentrations by as much as 20–30 ppbv. In contrast, along the northern and western boundaries, the global models generally produce 4–20 ppbv higher O_3 concentrations than the BASE scenario, accompanied by greater inter-model variability. Among them, H-CMAQ and GEOS-Chem show relatively similar patterns, whereas CESM2.2 exhibits substantially higher O_3 levels, particularly along the western boundary (Fig. 2 and Table 1).

Conversely, compared to the BASE scenario, the differences in boundary O_3 concentrations among the three global models significantly increase in the mid-to-upper troposphere (3–10 km) and stratosphere (above 10 km). In the mid-to-upper troposphere (3–10 km), the BASE scenario generally underestimates O_3 concentrations along the northern and western boundaries, while significantly overestimates them along the southern boundary. The CESM2.2 scenario shows higher O_3 concentrations along the eastern, northern, and western boundaries. In the stratosphere (above 10 km), the global model results indicate that the BASE scenario significantly overestimates O_3 concentrations along the southern, eastern, and western boundaries, with GEOS-Chem exhibiting the lowest O_3 concentrations among the four scenarios. The H-CMAQ and CESM2.2 models show large areas of high O_3 concentration near the northern boundary. These spatial variations in O_3 boundary conditions are likely to have a considerable impact on the simulation of surface O_3 concentrations over China during the summer months.

3.2 Evaluation of Model Performance Using Different CBC

3.2.1 Meteorological simulation evaluation

Table 2 presents an evaluation of WRF model simulations of 2 m temperature ($T2$), 2 m daily maximum temperature ($T2$max), 2 m relative humidity (RH2), 10 m wind speed (WS10), surface pressure (PRS), and precipitation (PRECIP). The data were averages from 2439 meteorological stations across China. Analysis of mean bias (MB), correlation coefficient (r), and index of agreement (IOA) reveals that the WRF model accurately simulated the meteorolog-

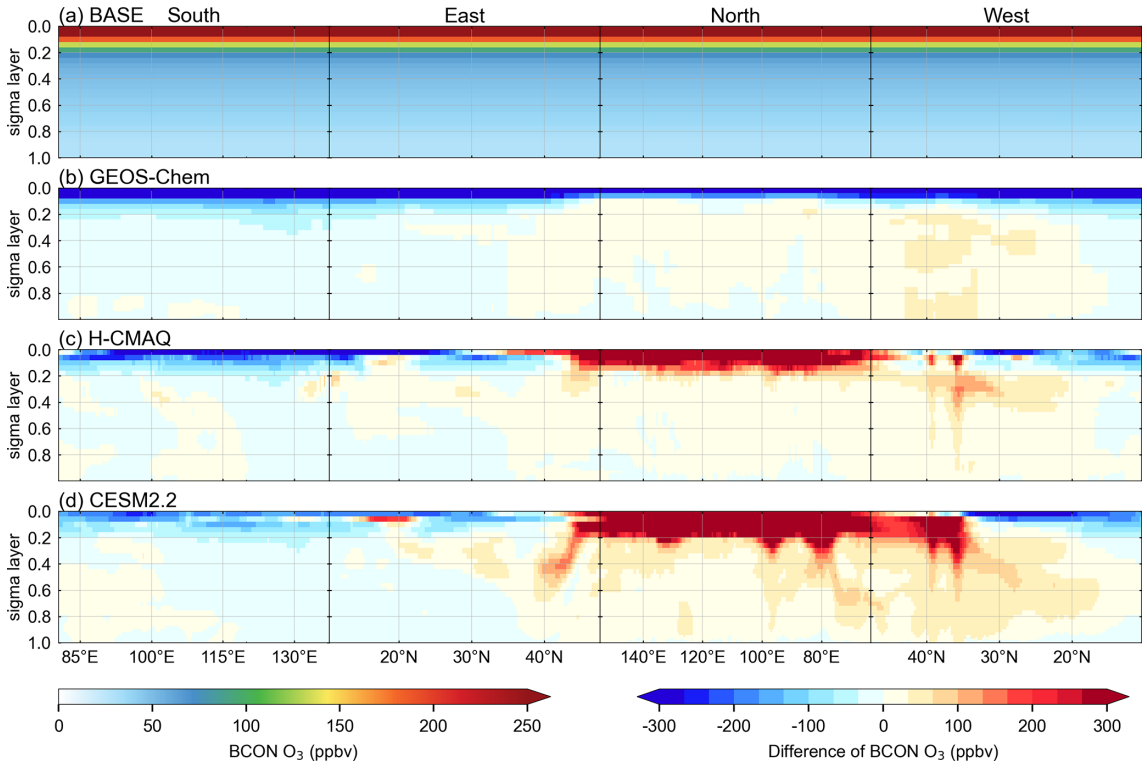

Figure 2. Temporally averaged O_3 chemical boundary conditions along the lateral boundaries of the CMAQ modeling domain. Panels show **(a)** BASE scenario O_3 concentrations, **(b)** GEOS-CHEM minus BASE, **(c)** H-CMAQ minus BASE, and **(d)** CESM2.2 minus BASE. Values are plotted clockwise, starting from the southwest corner of the CMAQ simulation domain, with the model's sigma coordinates.

Table 1. Statistical results of average O_3 concentrations (ppbv) at various vertical heights among the four boundaries for four CBC scenarios.

Vertical altitude	Boundary	BASE	H-CMAQ	GEOS-Chem	CESM2.2
0–3 km	South	31.7	27.3	25	26
	East	31.7	24.9	23.8	25.1
	North	31.7	39.5	36.4	47.4
	West	31.7	43.5	45.8	51.7
3–10 km	South	53.2	40.1	26.7	35.6
	East	53.2	54.9	43.4	61.7
	North	53.2	79.2	68.4	119.7
	West	53.2	76.2	60.6	88.7
Above 10 km	South	408.0	233.4	42.4	272.0
	East	408.0	351.6	82.0	373.8
	North	408.0	658.3	186.9	728.7
	West	408.0	338.6	88.2	324.1

ical fields. $T2$, $T2$max, RH2, and PRS exhibit IOA values exceeding 0.85, indicating strong agreement with observations. Correlation coefficients (r) exceed 0.7 for all variables except WS10. However, some biases remain in the simulation results for certain variables. Specifically, RH2 and PRS are slightly underestimated, while PRECIP is overestimated; nevertheless, the r and IOA values remain relatively high. In contrast, WS10 is significantly overestimated (by 1.6 m s^{-1}), with both IOA and r below 0.5. This likely stems from the relatively coarse model grid resolution, hindering accurate representation of urban topography and its impact on wind speed – a phenomenon observed in other studies (Hu et al., 2016; Shen et al., 2022). Overall, the WRF model demonstrates good performance in meteorological simulations, providing reliable inputs for the CMAQ model.

Table 2. Evaluation results for the meteorological variables.

Variable	OBS	SIM	MB	RMSE	IOA	r
$T2$ (°C)	25	24.4	−0.6	2.1	0.94	0.91
$T2$max (°C)	29.9	29.3	−0.6	2.5	0.91	0.86
RH2 (%)	73.6	69.1	−4.5	8.6	0.88	0.86
WS10 ($m\,s^{-1}$)	2	3.6	1.6	1.8	0.41	0.45
PRS (hPa)	937.8	922.7	−15.1	28.5	0.97	0.97
PRECIP (mm)	297.4	434.3	136.9	234.2	0.72	0.7

3.2.2 Surface O_3 Simulation Performance

Figure 3 illustrates the spatial distribution of avg-O3MDA8 and 90th-O3MDA8 concentrations and their normalized mean bias (NMB) across China. Across all monitoring sites, the observed avg-O3MDA8 and 90th-O3MDA8 for July-August 2019 are 59.4 and 82.8 ppbv, respectively (Table S3). Generally, O_3 concentrations in North China are higher than in South China. For 90th-O3MDA8, elevated values are widespread, notably in the North China Plain (NCP), Central China, Yangtze River Delta (YRD), Pearl River Delta (PRD), and Sichuan Basin (SCB), highlighting the severity of summer O_3 pollution across China.

Substantial discrepancies exist between observed and simulated O_3 across all CBC scenarios. The BASE scenario, in particular, systematically underestimates both mean and extreme O_3, especially in northern regions (latitude $> 30°$ N). Avg-O3MDA8 underestimations reach −16.1 ppbv in North China and −11.2 ppbv in Northwest China, with moderate underestimations in East (−5.1 ppbv) and Northeast China (−4.8 ppbv) (Fig. 3; Table S4). Similarly, 90th-O3MDA8 was underestimated by 32.9 % in North China and 26.2 % in Northwest China, with smaller NMB (−9.3 % to −14.2 %) elsewhere except South China (Table S5). These results indicate that the BASE scenario poorly represents both average and high O_3 levels, limiting its ability to capture O_3 formation and transport processes during hot seasons.

By incorporating global model-derived CBC, significant improvements in both bias and agreement are observed across China. Based on the NMB values for avg-O3MDA8 and 90th-O3MDA8 of all sites, the three dynamic CBC scenarios performance can be ranked as follows: GEOS-Chem (−0.3 %) > H-CMAQ (−1.1 %) > CESM2.2 (+4.9 %) for avg-O3MDA8 and CESM2.2 (−0.7 %) > GEOS-Chem (−6.5 %) > H-CMAQ (−7.9 %) for 90th-O3MDA8 (Tables S4–S5). GEOS-Chem consistently yields the smallest bias in avg-O3MDA8, indicating the most accurate representation of boundary and background O_3 inflow under average conditions. Notably, its normalized mean bias (NMB) falls within ±10 % in five of the seven subregions – specifically, all except North and Northwest China – demonstrating that the GEOS-Chem scenario best captures overall ozone levels across China. Correspondingly, its index of agreement (IOA) reaches 0.85 for avg-O3MDA8 and 0.83 for 90th-O3MDA8, the highest among all scenarios, suggesting excellent spatial and temporal consistency with observations. The H-CMAQ scenario also improves upon the BASE case, albeit to a slightly lesser extent, reducing O_3 underestimation while maintaining IOAs of 0.82 (avg-O3MDA8) and 0.81 (90th-O3MDA8). In contrast, the CESM2.2 scenario exhibits a positive NMB for avg-O3MDA8 (+4.9 %), suggesting a slight overestimation in background inflow. However, CESM2.2 substantially improved the simulation of O_3 extremes, with a much smaller NMB for all sites (−0.7 %)for 90th-O3MDA8. The underestimation of high ozone concentrations and pollution episodes is significantly alleviated in five subregions: North, Northeast, Northwest, East, and Southwest China. This improvement is further underscored by a consistently high IOA of 0.83, highlighting CESM2.2's capability in accurately reproducing high-O_3 pollution events – particularly in regions characterized by complex terrain and intense photochemical activity. Overall, these results demonstrate that applying dynamic CBC derived from global chemical transport models substantially enhances the simulation of both average and extreme O_3 concentrations. The CESM2.2 CBC may perform relatively better in simulating high ozone concentrations and pollution episodes.

At the regional scale, however, differences among the three dynamic CBC scenarios become regionally differentiated (Fig. 4). Although GEOS-Chem and H-CMAQ consistently show the best nationwide performance, CESM2.2 demonstrates superior accuracy in several regions. For instance, CESM2.2 achieves the smallest NMB and highest IOA in the north (N), northeast (NE), east (E) and northwest (NW) regions for both avg-O3MDA8 and 90th-O3MDA8, reflecting its strength in capturing high O_3 events in those areas. In the SW region, CESM2.2 outperforms other models with a positive NMB yet high IOA, indicating a well-aligned simulation of elevated background O_3 levels. In contrast, GEOS-Chem exhibits balanced performance across most regions, notably achieving relatively low NMB and high IOA in the east (E), central (C), and northeastern (NE) regions. These areas are typically influenced by continental outflow and moderate photochemistry, conditions under which GEOS-Chem's background O_3 input appears to be well-optimized. H-CMAQ offers moderate improvement relative to the BASE scenario across most regions, with less extreme biases than BASE and slightly lower IOA compared to CESM2.2 or GEOS-Chem.

3.2.3 Vertical O_3 profile Evaluation

To assess the performance of the model in simulating vertical O_3 distribution under different CBC, we compar the simulated O_3 profiles from the four scenarios with observational data from five ozonesonde stations (Fig. 5). To better evaluate model performance at different altitudes, we comput mean O_3 concentrations within three representative vertical layers:

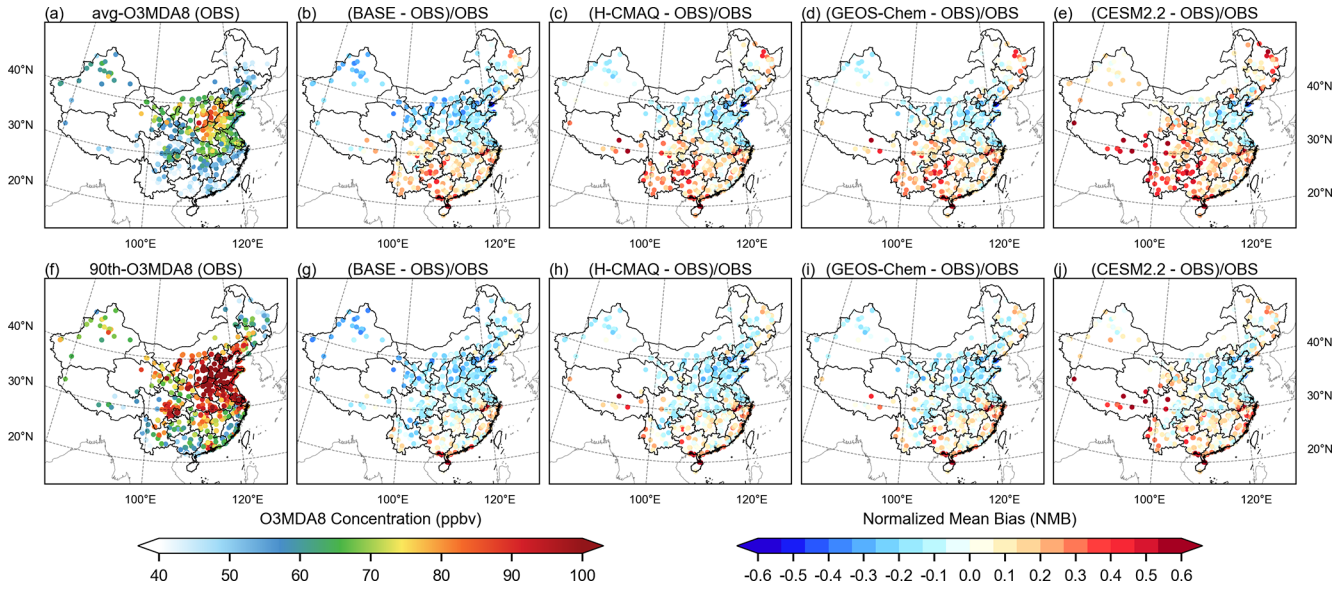

Figure 3. Spatial distribution of avg-O3MDA8 and 90th-O3MDA8 from observations (OBS) and four CBC scenario simulations. Panels **(a)** and **(f)** show observed avg-O3MDA8 and 90th-O3MDA8 at 1480 monitoring sites during July–August 2019, while panels **(b)**–**(e)** and **(g)**–**(j)** present site-level normalized mean bias (NMB) for BASE, H-CMAQ, GEOS-Chem, and CESM2.2 simulations, respectively.

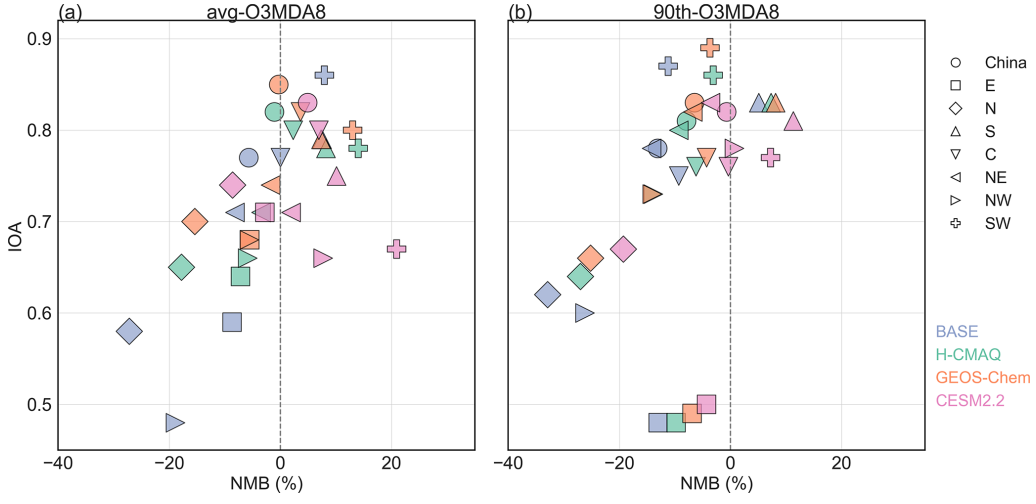

Figure 4. Comparison of model performance among four CBC scenarios (BASE, H-CMAQ, GEOS-Chem, and CESM2.2) in terms of Normalized Mean Bias (NMB, %) and Index of Agreement (IOA) for **(a)** average daily maximum 8 h O_3 concentrations (avg-O3MDA8) and **(b)** the 90th percentile of daily maximum 8 h O_3 (90th-O3MDA8) in China and its seven subregions (South (S), East (E), North (N), Central (C), Northeast (NE), Northwest (NW), and Southwest (SW)). Statistics are based on daily data from July–August 2019; number of monitoring sites: China (1480), E (319), N (181), S (256), C (204), NE (166), NW (154), and SW (200).

the lower troposphere (0–3 km), the middle-to-upper troposphere (3–10 km), and the lower stratosphere (10–16 km), as summarized in Table 3.

In lower troposphere (0–3 km), observed O_3 concentrations in this layer ranged from ∼ 39 to 65 ppbv across the five sites. O_3 concentrations in the lower troposphere are sensitive to both local emissions and background inflow. The BASE scenario generally underestimates O_3, whereas incorporating dynamic CBC increased near-surface concentrations. Among the scenarios, GEOS-Chem exhibits the most balanced performance, with mean biases typically within ±10 ppbv. CESM2.2 overestimates O_3 substantially at high-altitude sites, e.g., +25.0 ppbv at Lhasa and +9.7 ppbv at Golmud, indicating excessive inflow of near-surface O_3. H-CMAQ also slightly overestimates O_3, but with smaller magnitudes. These results indicate that while dynamic CBC improve near-surface O_3 representation, overestimation in clean

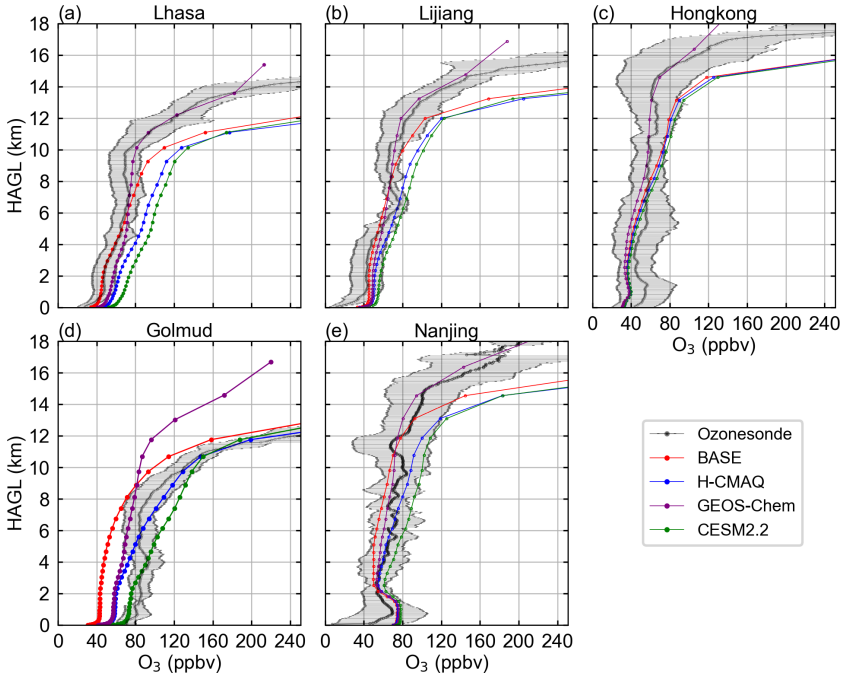

Figure 5. Comparison of vertical O_3 profiles between four CBC scenario simulation (BASE, H-CMAQ, GEOS-Chem, and CESM2.2) and sounding observations at five stations across China. All profiles are plotted against Height Above Ground Level (HAGL); statistics are based on vertical profile data summarized in Table S2 (including observation periods and site-specific information).

Table 3. Comparison and evaluation of vertical O_3 concentration profiles (ppbv) at each sounding station.

	Lhasa	Lijiang	Hongkong	Golmud	Nanjing
Lower troposphere (0–3 km)					
OBS	45.4	39.1	49.9	64.9	57.9
BASE	45.3	45.1	40.8	43.0	64.8
H-CMAQ	60.6	50.6	41.3	59.4	67.0
GEOS-Chem	54.8	48.8	39.5	57.5	67.3
CESM2.2	70.4	55.7	41.9	74.6	71.0
Mid-to-upper troposphere (3–10 km)					
OBS	66.7	62.1	53.9	85.0	68.2
BASE	75.1	62.0	51.4	62.7	56.1
H-CMAQ	94.9	74.8	53.9	94.7	71.5
GEOS-Chem	72.6	62.9	45.8	73.8	62.2
CESM2.2	104.0	81.4	56.7	112.0	83.5
Lower stratosphere (10–16 km)					
OBS	230.8	122.1	68.1	174.6	92.3
BASE	306.6	211.7	106.5	288.1	117.7
H-CMAQ	394.4	259.3	112.8	367.7	149.7
GEOS-Chem	147.5	106.6	66.8	131.8	85.7
CESM2.2	371.3	249.3	116.0	332.6	153.8

or elevated regions (e.g., Lhasa) must be carefully considered, especially when using CESM2.2.

The mid-to-upper troposphere (3∼10 km) reflects regional background transport, deep convection, and vertical mixing. Observed O_3 levels typically increase with altitude, ranging from ∼54 to 85 ppbv. The BASE scenario consistently underestimates O_3 in this layer, particularly in Golmud (−22.3 ppbv) and Nanjing (−12.1 ppbv), due to insufficient O_3 inflow. Dynamic CBC significantly reduces this bias. H-CMAQ and CESM2.2 both improve model–observation agreement, but CESM2.2 often overestimates O_3 (e.g., +37.3 ppbv in Lhasa), potentially reflecting overly strong entrainment of free-tropospheric O_3. GEOS-Chem again performs best overall, producing values close to observations in Lijiang, Nanjing, and Lhasa, demonstrating a good balance between under- and overestimation. This suggests that GEOS-Chem CBC offer the most realistic representation of free-tropospheric O_3, while CESM2.2 may be too aggressive in polluted or convective regions.

In the lower stratosphere (10–16 km), O_3 levels increase sharply in this layer, with observed values ranging from ∼68 to 231 ppbv. The BASE scenario significantly overestimates stratospheric O_3 at all sites, especially in Golmud and Lhasa, indicating excessive intrusion of stratospheric O_3 in default boundary inputs. This bias is further amplified in H-CMAQ and CESM2.2, with overestimations exceeding ∼164 and ∼140 ppbv in Lhasa and ∼193 and ∼158 ppbv in Golmud. From the vertical O_3 profile comparison, the elevated biases in the lower stratosphere of BASE, H-CMAQ, and CESM2.2 scenarios may enhance the stratosphere–troposphere exchange (STE), especially in southwestern and southern China, which is sig-

nificantly influenced by the Qinghai-Tibet Plateau (Fig. 5a–c, e). In contrast, GEOS-Chem was the only CBC that consistently reduced this overestimation, bringing modeled values closer to observations at all sites. For example, it lowers the stratospheric bias in Golmud from +113.5 ppbv (BASE) to −42.8 ppbv and achieved near-perfect agreement in Hong Kong (−1.3 ppbv). Overall, the vertical profile analysis underscores that GEOS-Chem provides the most accurate representation of upper tropospheric and stratospheric O_3 inflow, especially important for western China where STE processes are more active.

3.2.4 Satellite-Based O_3 Column Assessment

The spatial distribution of tropospheric ozone column (TOC) concentrations provides valuable insights into regional O_3 pollution patterns. In this study, TOC concentrations retrieved from the Environmental Trace Gases Monitoring Instrument (EMI) aboard the Gaofen-5 satellite during July–August 2019 were compared with simulation (SIM) results from four different scenario models (Fig. 6). Observational data from EMI indicate a general increase in TOC concentrations with latitude across China, consistent with previous studies (Zhu et al., 2022; Liu et al., 2022). North China exhibits the highest TOC values among the eastern regions, corresponding to areas known for severe surface-level O_3 pollution (Lu et al., 2018).

From the numerical modeling perspective, the simulation scenarios based on the BASE, H-CMAQ, and CESM2.2 models predominantly reflect an overestimation of TOC concentrations. Among them, the BASE scenario demonstrates the least degree of overestimation, particularly in the South China and Northeast China regions, where overestimations range from 20 to 30 DU, while other regions exhibit overestimations between 10 and 20 DU. Both the H-CMAQ and CESM2.2 models show robust overestimations exceeding 20 DU, especially in northern China (north of 35° N), where the overestimation can surpass 40 DU, with the Northeast region registering the highest overestimation, reaching beyond ∼ 50–60 DU. In contrast, the CBC boundary conditions provided by the GEOS-Chem model yield superior results in simulating the spatial distribution of TOC, with slight overestimations noted in South China and areas north of 40° N, while underestimating concentrations within the latitude range of 30 to 40° N. The regional mean bias (MB) of model-simulated TOC versus satellite observations was calculated for the mainland of China. The MB of model-simulated TOC (DU) for the four scenarios – BASE, H-CMAQ, CESM2.2, and GEOS-Chem – is 14.4, 40.4, 41.7, and 0.7 DU, respectively, consistent with the analysis results shown in Fig. 5. And the simulation discrepancies for TOC across China are confined to approximately ±10 DU, indicating that GEOS-Chem's CBC represent the optimal boundary condition input for regional O_3 modeling in China area.

3.3 Mechanism of the impact of CBC on O_3 formation

3.3.1 General impact of synoptic-scale circulation

CBC regulate regional O_3 by controlling the inflow of background O_3 and precursors at model boundaries. Given the superior performance of GEOS-Chem in reproducing surface and vertical O_3 based on our validations, we further contrast GEOS-Chem with the BASE scenario to highlight the role of CBC in cross-boundary transport at the surface and at 700, 500, and 200 hPa isobaric surfaces (Fig. 7).

In southeastern China, summer monsoonal flow carries relatively clean marine air into the mid–lower troposphere, lowering background O_3 and suppressing accumulation over eastern and southern regions, where GEOS-Chem boundary conditions produce slightly reduced concentrations (< 4 %, Fig. 7a–b). This dilution effect is consistent with the characteristic influence of the Western Pacific Subtropical High during summer, which effectively flushes the coastal boundary layer with cleaner oceanic air masses. In contrast, along the northern and western boundaries, GEOS-Chem introduces substantially higher O_3 than BASE. Advected by prevailing northwesterlies, these inflows penetrate deep into inland China, increasing surface O_3 by more than 10 % across most regions and by over 20 % in northern and northwestern China. The magnitude of this enhancement aligns with the recognized impact of long-range transport from Eurasia, which often elevates the ozone baseline in northern China. The influence of CBC is even stronger at higher altitudes (Fig. 7c–d). At 500 and 200 hPa, GEOS-Chem introduces markedly higher O_3 than BASE, reflecting enhanced background inflows and contributions from stratospheric air masses. This vertical gradient in CBC sensitivity underscores the role of the free troposphere as a reservoir for long-lived O_3. Such upper-level enhancements have important surface implications, as downward mixing and stratosphere–troposphere exchange (STE) can transport high-O_3 air into the boundary layer under favorable meteorological conditions, especially during the passage of cold fronts or deep convective mixing, further exacerbating pollution episodes.

Overall, these results highlight that the mechanistic impact of CBC on O_3 formation arises from a synergistic combination of boundary inflow composition and large-scale circulation. While oceanic inflows tend to dilute O_3 in southern and eastern regions, strong continental and stratospheric inflows from the north and west can significantly elevate both free-tropospheric and surface O_3, amplifying pollution severity in inland China. These findings confirm that accurate CBC are not merely a model constraint but a vital component for capturing the dynamic interplay between local photochemistry and global atmospheric circulation.

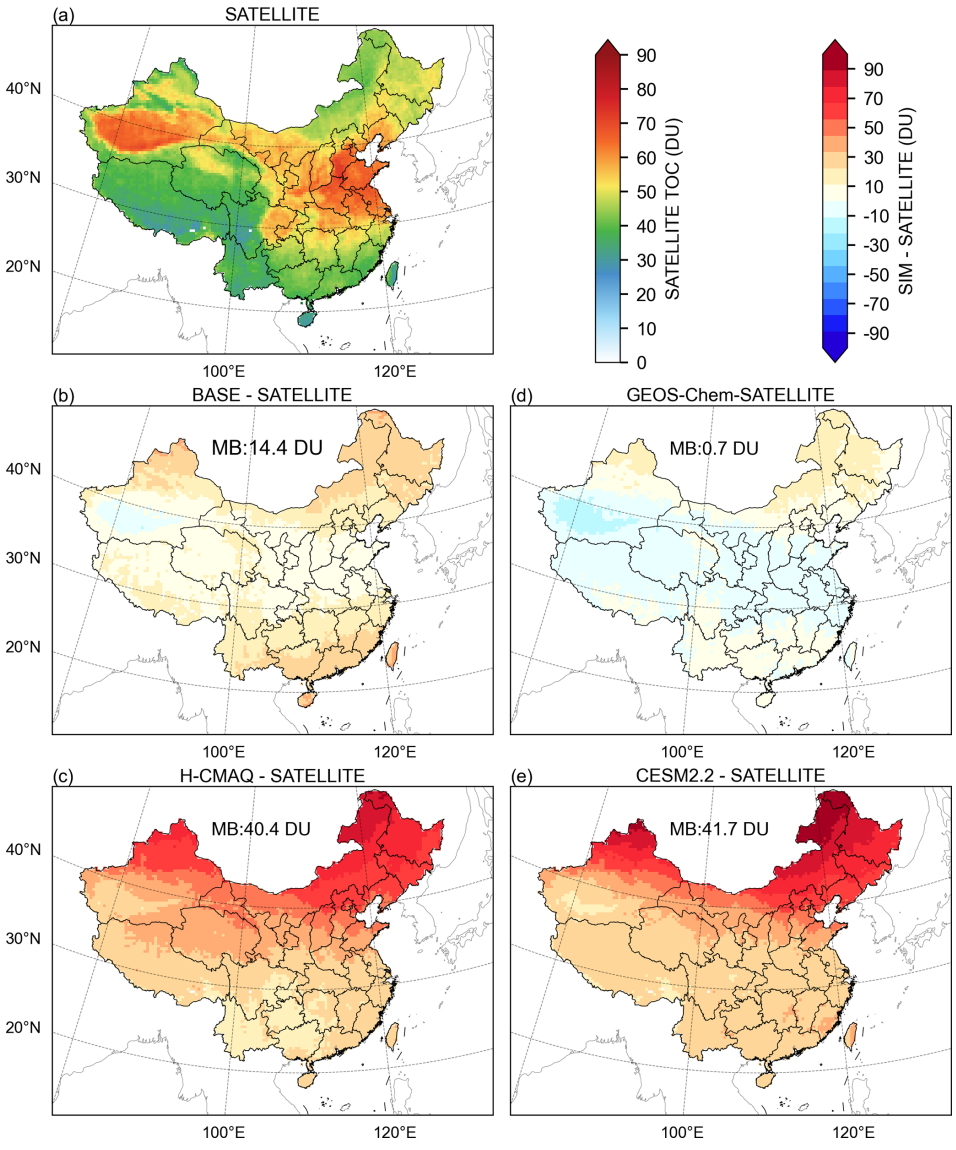

Figure 6. Comparison of tropospheric ozone column (TOC) distributions over China between satellite observations and model simulations. Panel **(a)** shows the TOC retrieved from satellite measurements, while panels **(b)–(e)** depict the differences (MB) between simulated TOC from the BASE, H-CMAQ, GEOS-Chem, and CESM2.2 scenarios and the satellite retrieval.

3.3.2 Case Study: Synoptic-Scale Circulation Dynamics Modulating CBC Impacts

The influence of CBC varies dynamically with large-scale meteorological conditions rather than remaining static. During summer, synoptic disturbances such as the Western Pacific Subtropical High extensions, tropical cyclone activity, and East Asian westerly jet fluctuations reshape regional circulation patterns and modulate the transport of polluted or clean air masses into the model domain. These circulation changes, characterized by alternating cyclonic and anticyclonic flows, substantially alter the efficiency of transboundary transport and consequently affect CBC impacts on near-surface O_3 simulations. Here, we examine two sequential circulation regimes during August 2019 associated with successive typhoon events: Super Typhoon Lekima and Typhoon Krosa. These events create distinctly different transport patterns that modulated how boundary conditions influenced surface O_3 across China. Based on this evolution, we define two phases: Phase 1 (P1, 10–14 August, during Lekima's landfall and decay in Eastern China) and Phase 2 (P2, 15–19 August, controlled by post-trough northwesterlies) (Fig. 8).

P1 occurs during the landfall and decay of Super Typhoon Lekima over the Yangtze River Delta (Figs. 8a, b and S2). The tropospheric circulation is dominated by a deep trough linked to the typhoon's remnant system, which enhances southeasterly flow of marine air into eastern China. This pat-

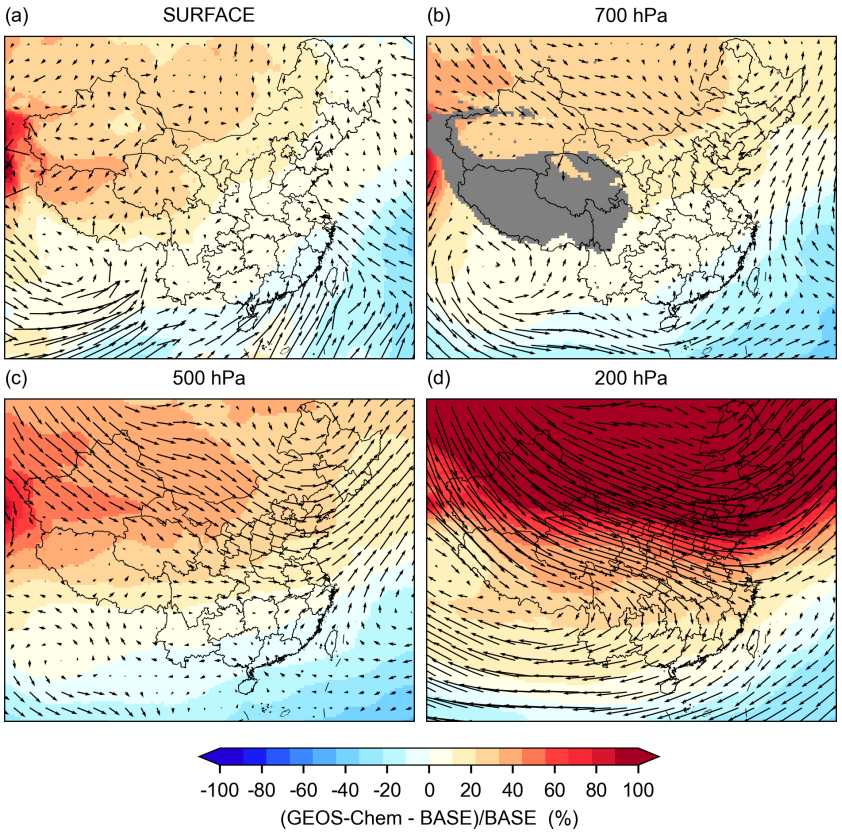

Figure 7. Normalized mean bias (NMB, (GEOS-Chem − BASE) / BASE) of mean O_3 concentrations and corresponding mean flow fields at surface and 700, 500, and 200 hPa isobaric surfaces over the simulation domain. (The grey area indicates invalid value.)

tern promotes deep convection and vigorous vertical mixing, leading to a pronounced coastal-inland gradient in surface O_3: marine-influenced coastal areas exhibit low concentrations (< 50 ppbv), while inland regions maintain moderate-to-high levels (60–90 ppbv). The cyclonic circulation disrupts typical westerly transport pathways, reducing transboundary O_3 influence from northern and western source regions. Consequently, the BASE scenario overestimates O_3 by 15–25 ppbv over oceanic regions where static boundary conditions fail to capture typhoon-enhanced marine influence, while underestimating concentrations by 10–20 ppbv in northwestern China where continental transport remains active but was inadequately represented by the Pacific-based boundary profile (Fig. 8b).

By contrast, P2 is characterized by a dominant northwesterly flow across central and eastern China, situated behind a mid-level trough, while a high-pressure system strengthened over western China (Fig. 8c–d). This "east-trough, west-ridge" configuration facilitates the efficient advection of O_3-rich air from western and northern source regions, resulting in the noticeable O_3 elevations observed across the region (Fig. 8c–d). Model sensitivity analysis confirms that accurately representing these high-O_3 boundary inflows under such transport-favorable conditions elevates surface concentrations by 10–15 ppbv in the most affected areas (Fig. 8d). These results demonstrate that the BASE scenario, employing static boundary conditions, systematically underestimates cross-boundary pollution contributions during dynamically active periods when long-range transport is of importance.

The difference between P2 and P1 (Fig. 8e–f) illustrates a marked meteorological transition from a pollution-scavenging cyclonic regime during P1 to a pollution-accumulating regime in P2, characterized by trough-driven northwesterly transport and high-pressure-induced stability. This synoptic shift corresponds with observed surface O_3 increases of 30–60 ppbv across northern and central-eastern China. These regions align spatially with the anticyclonic circulation, where enhanced subsidence favors the accumulation of transported O_3. By incorporating chemically realistic CBC, the simulation attributes approximately 10 ppbv of this O_3 increase to cross-boundary transport during P2 (Fig. 8f), highlighting the essential role of CBC in accurately capturing O_3 buildup under transport-favorable synoptic regimes.

To further clarify the role of dynamic CBC in O_3 simulations, we perform vertical cross-sectional analyses using the CMAQ process analysis module along the major transport pathways during P1 and P2 (Fig. 9). Both phases con-

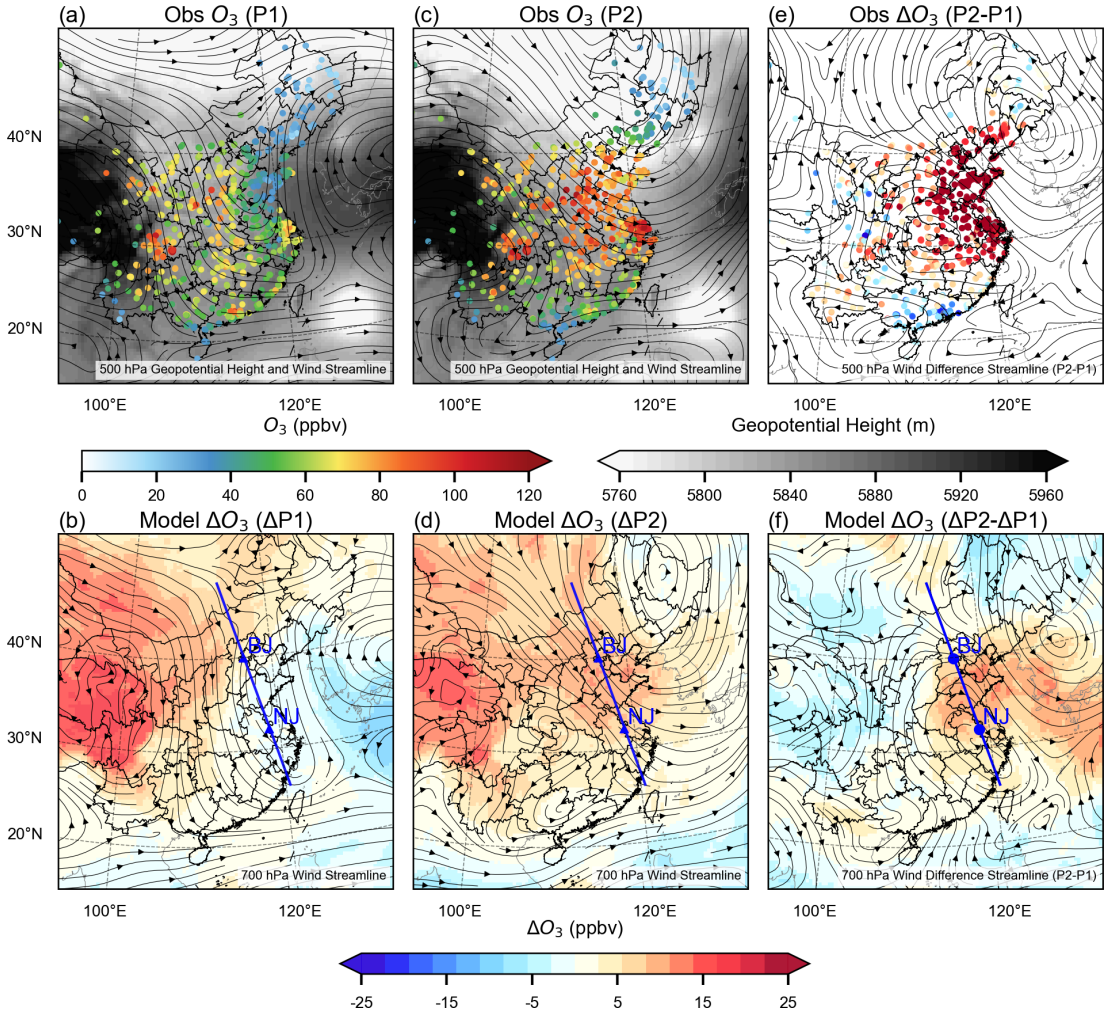

Figure 8. **(a)** Distribution of 500 hPa winds (streamlines), geopotential height (contours), and surface O_3 observations (dots) during P1; **(b)** distribution of 700 hPa winds (streamlines), and difference in modeled surface O_3 between GEOS-Chem CBC and BASE during P1; **(c)** same as panel **(a)** but for P2; **(d)** same as panel **(b)** but for P2; **(e)** differences in observed surface O_3 and 500 hPa winds between P1 and P2; **(f)** differences in simulated surface O_3 and 700 hPa winds between P1 and P2. Blue lines indicate the locations of vertical cross-sectional analyses, extending from north to south through Beijing (BJ) and Nanjing (NJ).

sistently reveal strong cross-boundary transport, with upstream inflows from outside the domain substantially influencing downstream O_3 levels across mainland China. During P1, Typhoon Lekima disrupts the transport corridor near the Yangtze River Delta (approximately 0–4 km), restricting cross-boundary influences mainly to northern inflows affecting the North China Plain (Fig. 9a). In contrast, under post-trough northwesterly flow during P2, cross-boundary transport extends southward from the northern boundary, reaching as far as the Yangtze River Delta (Fig. 9b). The difference between P1 and P2 highlights a distinct transport corridor extending from higher to lower latitudes and from the mid–upper troposphere toward the surface (Fig. S3), further emphasizing the crucial role of dynamic CBC in shaping O_3 distributions.

Here, we demonstrate that cross-boundary transport also occurs in the vertical dimension, with O_3-rich air descending from the upper to the lower troposphere, while stratosphere–troposphere exchange (STE) provides an additional pathway for transboundary inflow. To identify possible STE occurrences, potential vorticity (PV) between 10 and 14 km (above sea level) is examined, adopting a threshold of 2 PVU (PV units, $1\,\mathrm{PVU} = 10^{-6}\,\mathrm{m^{-2}\,s^{-1}\,kg^{-2}}$) to distinguish stratospheric from tropospheric air masses. STE events are evident over northern China during both P1 and P2 (Figs. 9c–d and S4). In addition, the CMAQ process analyses with GEOS-Chem CBC corroborate intensified vertical transport between 10 and 14 km in both phases, with distinctly positive contributions from vertical advection and turbulent diffusion. As a result, the joint impact of large-scale advection and vertical mixing processes enables high-altitude O_3 to intrude into the

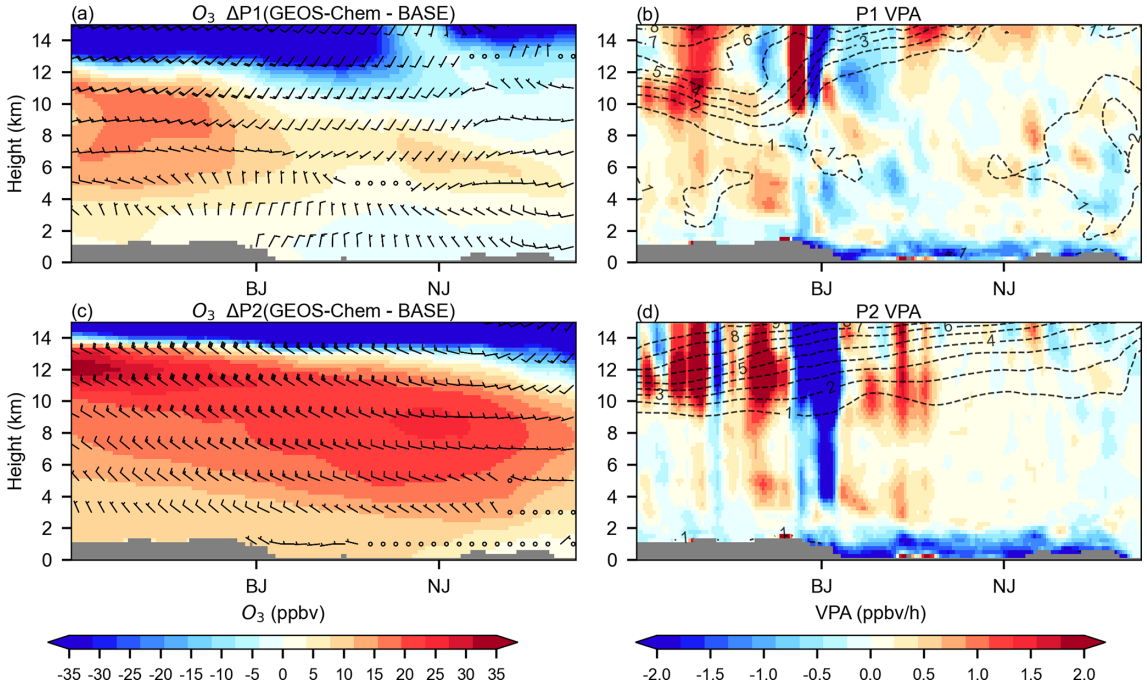

Figure 9. **(a)** Vertical cross-sectional analysis of the O_3 difference between GEOS-Chem CBC and the BASE scenario during P1, the wind bar denotes vertical wind field; **(b)** vertical distribution of potential vorticity (PV, dashed contours) and vertical transport (VPA, calculated by CMAQ process analysis as the sum of vertical diffusion and vertical advection) during P1; **(c)** same as panel **(a)** but for P2. **(d)** Same as panel **(b)** but for P2. The x-axis labels BJ and NJ indicate the locations of Beijing and Nanjing, respectively.

lower troposphere and ultimately affect downstream regions, even in YRD (such as Nanjing city).

4 Conclusion

This research demonstrates that CBC represent a critical but often underappreciated component of regional air quality modeling systems. We systematically evaluated the influence of CBC on regional O_3 simulations over China using the WRF-CMAQ model. Four CBC scenarios were compared: a static BASE scenario using climatological profiles and three dynamic scenarios derived from global chemical transport models (H-CMAQ, GEOS-Chem, and CESM2.2). Overall, dynamic CBC substantially improve the representation of surface O_3 compared to the static BASE scenario, with GEOS-Chem CBC performing the best. Across China, the normalized mean bias (NMB) for avg-O3MDA8 is reduced from −5.7 % (BASE) to −0.3 % (GEOS-Chem), and the IOA increased from 0.77 to 0.85, while the 90th-O3MDA8 percentile NMB improved from −13.1 % to −6.5 %, and the IOA increased from 0.66 to 0.77. Based on ozonesonde profiles and satellite TOC evaluations, elevated biases are identified in the lower stratosphere for BASE, H-CMAQ, and CESM2.2, which may lead to overestimation of background O_3 concentrations, particularly during STE events.

The influence of CBC varies dynamically with large-scale meteorological conditions rather than remaining static. During summer, synoptic disturbances such as the Western Pacific Subtropical High extensions, tropical cyclone activity, and East Asian westerly jet fluctuations reshape regional circulation patterns and modulate the transport of polluted or clean air masses into the model domain. These circulation changes, characterized by alternating cyclonic and anticyclonic flows, substantially alter the efficiency of transboundary transport and consequently affect CBC impacts on near-surface O_3 simulations. Generally, oceanic inflows from the south dilute O_3 in southeastern and coastal areas, whereas strong continental and stratospheric inflows from northern and western boundaries significantly modulate tropospheric O_3, especially in downwind regions of the synoptic systems.

A comparative analysis of two successive synoptic regimes in July–August 2019, which shifted from a cyclone-dominated, pollution-scavenging phase to a post-trough northwesterly flow favorable for accumulation, reveals that dynamic circulation patterns enhance cross-boundary transport both horizontally (via continental inflows from northern and western boundaries) and vertically (via stratosphere–troposphere exchange). The combined effects of these transport processes increase O_3 concentrations by 10 %–20 % during high-pollution events over eastern China. These results underscore that accurate representation of dynamic CBC is essential to capture circulation-driven horizontal and vertical transport and their integrated impact on regional O_3 distributions. Regarding the representativeness of these findings,

while this study focuses on summer 2019, the selected period captures representative meteorological regimes of the East Asian summer monsoon, including typical southeasterly marine flows and northwesterly continental inflows. The inclusion of typhoon-induced circulation changes (e.g., Lekima and Krosa) further ensures that the findings reflect common synoptic disturbances affecting regional air quality. Although quantitative magnitudes may vary with interannual climate variability, the identified mechanisms regarding CBC sensitivity under transport-favorable conditions are applicable to typical summer pollution episodes in monsoon-affected regions.

Our findings demonstrate that the choice of CBC is not merely a technicality but a dynamic determinant of simulated O_3 levels for regional CTM, especially when facing synoptic regimes that favor long-range transport or vertical exchange. This underscores the necessity of moving beyond static boundary conditions in regional air quality modeling. Static CBC remain a common baseline in regional modeling, with recent assessments indicating that a majority of studies still rely on default or unspecified boundary conditions (Zhu et al., 2024). While the simplified BASE scenario may not represent the most realistic boundary condition, it serves as a controlled baseline to isolate the incremental value of time-varying CBC, which is the primary focus of this study. To advance predictive capability, future efforts should pursue multi-model ensembles to quantify CBC uncertainty, evaluate 3-D climatological boundary conditions as a refined benchmark and explore the integration of real-time global fields into regional CTM forecasting systems. By elucidating the critical interplay between large-scale transport and regional pollution, this study provides a scientific foundation not only for improving O_3 forecasting but also for designing effective transboundary air quality management strategies.

Code and data availability. The observational datasets used in this study are publicly available from the following sources: surface meteorological data from the China Meteorological Administration (http://data.cma.cn); surface O_3 concentrations from the China National Environmental Monitoring Center (https://air.cnemc.cn:18007); ozonesonde profiles from the World Ozone and Ultraviolet Radiation Data Centre (WOUDC, https://woudc.org, last access: 4 April 2026), the China Air Pollution Data Center (CAPDC, https://www.capdatabase.cn), and the National Tibetan Plateau Data Center (TPDC, https://data.tpdc.ac.cn, last access: 4 April 2026); and tropospheric O_3 column data from the EMI/GF-5 product (http://222.173.100.190:9000/data-details, last access: 7 May 2026; Zhao et al., 2024). Meteorological boundary conditions data derived from the ERA5 reanalysis dataset are available at https://doi.org/10.24381/cds.adbb2d47 (Hersbach et al., 2023). The MEIC v1.4 and MIX v1.1 emission inventories are available at http://meicmodel.org. Global chemical model outputs used as boundary conditions are available from the EQUATES project (H-CMAQ, https://www.epa.gov/cmaq/EQUATES), GEOS-Chem (https://geoschem.github.io/), and CESM2.2/CAM-chem (https://www2.acom.ucar.edu/gcm/cam-chem). The WRF v3.9.1 (https://github.com/wrf-model/WRF, last access: 4 April 2026) and CMAQ v5.3.3 (https://github.com/USEPA/CMAQ) model source codes are open-source and publicly accessible via their official GitHub repositories. The custom scripts developed for processing global model outputs into CMAQ-compatible boundary conditions have been archived in the Zenodo repository under DOI: https://doi.org/10.5281/zenodo.19447294 (Du, 2026). Additional model results are stored on Shuguang high-performance computing system and available from the corresponding author upon reasonable request (nan.wang@scu.edu.cn).

Supplement. The supplement related to this article is available online at https://doi.org/10.5194/acp-26-6223-2026-supplement.

Author contributions. N.W. and F.Y. designed the research. Y.D. conducted the simulation. Y.D. and N.W. wrote the manuscript. S.L., Y.H., B.L. and G.S. contributed to the interpretation of the results. R.H., B.L., Y.J., N.W. and Y.F. provided critical feedback and helped to improve the manuscript.

Competing interests. The contact author has declared that none of the authors has any competing interests.

Disclaimer. Publisher's note: Copernicus Publications remains neutral with regard to jurisdictional claims made in the text, published maps, institutional affiliations, or any other geographical representation in this paper. The authors bear the ultimate responsibility for providing appropriate place names. Views expressed in the text are those of the authors and do not necessarily reflect the views of the publisher.

Acknowledgements. This research is supported by the National Key Research and Development Program (grant no. 2023YFC3709301), the National Natural Science Foundation Project (grant no. 42575120), the Youth Fund Project of the Sichuan Provincial Natural Science Foundation (24NSFSC2988), the Fundamental Research Funds for the Central Universities (Grant No. YJ202313). We acknowledge use of the hyperspectral remote sensing products of atmospheric compositions developed by Prof. Cheng Liu's group at the University of Science and Technology of China. Numerical computations were performed on Hefei advanced computing center. We also thank the Tsinghua University for developing and sharing the MEIC emission inventory.

Financial support. This research is supported by the National Key Research and Development Program (grant no. 2023YFC3709301), the National Natural Science Foundation Project (grant no. 42575120), the Youth Fund Project of the Sichuan Provincial Natural Science Foundation (grant no. 24NSFSC2988), the Fundamental Research Funds for the Central Universities (grant no. YJ202313).

Review statement. This paper was edited by Dantong Liu and reviewed by three anonymous referees.

References

Bai, L., Wang, J., Ma, X., and Lu, H.: Air pollution forecasts: An overview, Int. J. Env. Res. Pub. He., 15, 780, https://doi.org/10.3390/ijerph15040780, 2018.

Bai, Z.: Lhasa SWOP atmospheric composition comprehensive sounding data set (2019–2020), National Tibetan Plateau/Third Pole Environment Data Center [data set], https://doi.org/10.11888/Atmos.tpdc.300007, 2022.

Bai, Z. and Bian, J.: Golmud site SWOP atmospheric composition agent open line data (2020–2021), National Tibetan Plateau/Third Pole Environment Data Center [data set], https://doi.org/10.11888/Atmos.tpdc.300057, 2022a.

Bai, Z. and Bian, J.: Lijiang SWOP atmospheric composition comprehensive sounding data set (2021–2022), National Tibetan Plateau/Third Pole Environment Data Center [data set], https://doi.org/10.11888/Atmos.tpdc.300156, 2022b.

Byun, D. and Schere, K. L.: Review of the governing equations, computational algorithms, and other components of the Models-3 Community Multiscale Air Quality (CMAQ) modeling system, Appl. Mech. Rev., 59, 51–77, 2006.

Campbell, P. C., Bash, J. O., and Spero, T. L.: Updates to the Noah land surface model in WRF-CMAQ to improve simulated meteorology, air quality, and deposition, J. Adv. Model. Earth Sy., 11, 231–256, 2019.

Carter, W. P. and Heo, G.: Development of revised SAPRC aromatics mechanisms, Atmos. Environ., 77, 404–414, 2013.

Chiu, Y.-H. M., Wilson, A., Hsu, H.-H. L., Jamal, H., Mathews, N., Kloog, I., Schwartz, J., Bellinger, D. C., Xhani, N., and Wright, R. O.: Prenatal ambient air pollutant mixture exposure and neurodevelopment in urban children in the Northeastern United States, Environ. Res., 233, 116394, https://doi.org/10.1016/j.envres.2023.116394, 2023.

Dou, X., Yu, S., Li, J., Sun, Y., Song, Z., Yao, N., and Li, P.: The WRF-CMAQ Simulation of a Complex Pollution Episode with High-Level O_3 and PM2.5 over the North China Plain: Pollution Characteristics and Causes, Atmosphere, 15, 198, https://doi.org/10.3390/atmos15020198, 2024.

Du, Y.: CBC-Prep-CMAQ: Preprocessing Scripts and Key Outputs for Chemical Boundary Condition Sensitivity Simulations of Summer Ozone over China, Zenodo [code], https://doi.org/10.5281/zenodo.19447294, 2026.

Eastham, S. D., Weisenstein, D. K., and Barrett, S. R.: Development and evaluation of the unified tropospheric–stratospheric chemistry extension (UCX) for the global chemistry-transport model GEOS-Chem, Atmos. Environ., 89, 52–63, 2014.

Foley, K. M., Pouliot, G. A., Eyth, A., Aldridge, M. F., Allen, C., Appel, K. W., Bash, J. O., Beardsley, M., Beidler, J., and Choi, D.: 2002–2017 anthropogenic emissions data for air quality modeling over the United States, Data in Brief, 47, 109022, https://doi.org/10.1016/j.dib.2023.109022, 2023.

Gao, C., Zhang, X., Xiu, A., Tong, Q., Zhao, H., Zhang, S., Yang, G., Zhang, M., and Xie, S.: Intercomparison of multiple two-way coupled meteorology and air quality models (WRF v4.1.1–CMAQ v5.3.1, WRF–Chem v4.1.1, and WRF v3.7.1–CHIMERE v2020r1) in eastern China, Geosci. Model Dev., 17, 2471–2492, https://doi.org/10.5194/gmd-17-2471-2024, 2024.

Geng, G., Liu, Y., Liu, Y., Liu, S., Cheng, J., Yan, L., Wu, N., Hu, H., Tong, D., and Zheng, B.: Efficacy of China's clean air actions to tackle PM2.5 pollution between 2013 and 2020, Nat. Geosci., 17, 987–994, 2024.

Godowitch, J. M., Gilliam, R. C., and Roselle, S. J.: Investigating the impact on modeled ozone concentrations using meteorological fields from WRF with an updated four–dimensional data assimilation approach, Atmos. Pollut. Res., 6, 305–311, 2015.

Goldberg, D. L., Vinciguerra, T. P., Hosley, K. M., Loughner, C. P., Canty, T. P., Salawitch, R. J., and Dickerson, R. R.: Evidence for an increase in the ozone photochemical lifetime in the eastern United States using a regional air quality model, J. Geophys. Res.-Atmos., 120, 12778–12793, 2015.

Grell, G. A., Peckham, S. E., Schmitz, R., McKeen, S. A., Frost, G., Skamarock, W. C., and Eder, B.: Fully coupled "online" chemistry within the WRF model, Atmos. Environ., 39, 6957–6975, 2005.

Hersbach, H., Bell, B., Berrisford, P., Biavati, G., Horányi, A., Muñoz Sabater, J., Nicolas, J., Peubey, C., Radu, R., Rozum, I., Schepers, D., Simmons, A., Soci, C., Dee, D., and Thépaut, J.-N.: ERA5 hourly data on single levels from 1940 to present, Copernicus Climate Change Service (C3S) Climate Data Store (CDS) [data set], https://doi.org/10.24381/cds.adbb2d47, 2023.

Hogrefe, C., Liu, P., Pouliot, G., Mathur, R., Roselle, S., Flemming, J., Lin, M., and Park, R. J.: Impacts of different characterizations of large-scale background on simulated regional-scale ozone over the continental United States, Atmos. Chem. Phys., 18, 3839–3864, https://doi.org/10.5194/acp-18-3839-2018, 2018.

Hu, J., Chen, J., Ying, Q., and Zhang, H.: One-year simulation of ozone and particulate matter in China using WRF/CMAQ modeling system, Atmos. Chem. Phys., 16, 10333–10350, https://doi.org/10.5194/acp-16-10333-2016, 2016.

Jacob, D. J.: The oxidizing power of the atmosphere, Handbook of weather, climate and water, 29–46, ISBN 978-0-471-21489-2, 2003.

Jerrett, M., Arain, A., Kanaroglou, P., Beckerman, B., Potoglou, D., Sahsuvaroglu, T., Morrison, J., and Giovis, C.: A review and evaluation of intraurban air pollution exposure models, J. Expo. Sci. Env. Epid., 15, 185–204, 2005.

Lei, Y., Wu, K., Zhang, X., Kang, P., Du, Y., Yang, F., Fan, J., and Hou, J.: Role of meteorology-driven regional transport on O_3 pollution over the Chengdu Plain, southwestern China, Atmos. Res., 285, https://doi.org/10.1016/j.atmosres.2023.106619, 2023.

Li, M., Liu, H., Geng, G., Hong, C., Liu, F., Song, Y., Tong, D., Zheng, B., Cui, H., and Man, H.: Anthropogenic emission inventories in China: a review, Nat. Sci. Rev., 4, 834–866, 2017a.

Li, M., Zhang, Q., Kurokawa, J.-I., Woo, J.-H., He, K., Lu, Z., Ohara, T., Song, Y., Streets, D. G., Carmichael, G. R., Cheng, Y., Hong, C., Huo, H., Jiang, X., Kang, S., Liu, F., Su, H., and Zheng, B.: MIX: a mosaic Asian anthropogenic emission inventory under the international collaboration framework of the MICS-Asia and HTAP, Atmos. Chem. Phys., 17, 935–963, https://doi.org/10.5194/acp-17-935-2017, 2017b.

Liu, J., Strode, S. A., Liang, Q., Oman, L. D., Colarco, P. R., Fleming, E. L., Manyin, M. E., Douglass, A. R., Ziemke, J. R., and Lamsal, L. N.: Change in tropospheric ozone

in the recent decades and its contribution to global total ozone, J. Geophys. Res.-Atmos., 127, e2022JD037170, https://doi.org/10.1029/2022JD037170, 2022.

Lu, X., Hong, J., Zhang, L., Cooper, O. R., Schultz, M. G., Xu, X., Wang, T., Gao, M., Zhao, Y., and Zhang, Y.: Severe surface ozone pollution in China: a global perspective, Environ. Sci. Technol. Lett., 5, 487-494, 2018.

Lu, X., Zhang, L., Wang, X., Gao, M., Li, K., Zhang, Y., Yue, X., and Zhang, Y.: Rapid increases in warm-season surface ozone and resulting health impact in China since 2013, Environ. Sci. Technol. Lett., 7, 240–247, 2020.

Mallard, M. S., Spero, T. L., and Taylor, S. M.: Examining WRF's sensitivity to contemporary land-use datasets across the contiguous United States Using Dynamical Downscaling, J. Appl. Meteorol. Clim., 57, 2561–2583, 2018.

Malley, C. S., Henze, D. K., Kuylenstierna, J. C., Vallack, H. W., Davila, Y., Anenberg, S. C., Turner, M. C., and Ashmore, M. R.: Updated global estimates of respiratory mortality in adults ≥ 30 years of age attributable to long-term ozone exposure, Environ. Health Persp., 125, 087021, https://doi.org/10.1289/EHP1390, 2017.

Mao, J., Fan, S., Jacob, D. J., and Travis, K. R.: Radical loss in the atmosphere from Cu-Fe redox coupling in aerosols, Atmos. Chem. Phys., 13, 509–519, https://doi.org/10.5194/acp-13-509-2013, 2013.

Mao, J., Li, L., Li, J., Sulaymon, I. D., Xiong, K., Wang, K., Zhu, J., Chen, G., Ye, F., and Zhang, N.: Evaluation of long-term modeling fine particulate matter and ozone in China during 2013–2019, Front. Environ. Sci., 10, 872249, https://doi.org/10.3389/fenvs.2022.872249, 2022a.

Mao, M., Rao, L., Jiang, H., He, S., and Zhang, X.: Air pollutants in metropolises of eastern coastal China, Int. J. Env. Res. Pub. He., 19, 15332, https://doi.org/10.3390/ijerph192215332, 2022b.

Monks, P. S., Archibald, A. T., Colette, A., Cooper, O., Coyle, M., Derwent, R., Fowler, D., Granier, C., Law, K. S., Mills, G. E., Stevenson, D. S., Tarasova, O., Thouret, V., von Schneidemesser, E., Sommariva, R., Wild, O., and Williams, M. L.: Tropospheric ozone and its precursors from the urban to the global scale from air quality to short-lived climate forcer, Atmos. Chem. Phys., 15, 8889–8973, https://doi.org/10.5194/acp-15-8889-2015, 2015.

Ni, R., Lin, J., Yan, Y., and Lin, W.: Foreign and domestic contributions to springtime ozone over China, Atmos. Chem. Phys., 18, 11447–11469, https://doi.org/10.5194/acp-18-11447-2018, 2018.

Park, R. J., Jacob, D. J., Field, B. D., Yantosca, R. M., and Chin, M.: Natural and transboundary pollution influences on sulfate-nitrate-ammonium aerosols in the United States: Implications for policy, J. Geophys. Res.-Atmos., 109, https://doi.org/10.1029/2003JD004473, 2004.

Parrella, J. P., Jacob, D. J., Liang, Q., Zhang, Y., Mickley, L. J., Miller, B., Evans, M. J., Yang, X., Pyle, J. A., Theys, N., and Van Roozendael, M.: Tropospheric bromine chemistry: implications for present and pre-industrial ozone and mercury, Atmos. Chem. Phys., 12, 6723–6740, https://doi.org/10.5194/acp-12-6723-2012, 2012.

Sahu, S. K., Liu, S., Liu, S., Ding, D., and Xing, J.: Ozone pollution in China: Background and transboundary contributions to ozone concentration & related health effects across the country, Sci. Total Environ., 761, 144131, https://doi.org/10.1016/j.scitotenv.2020.144131, 2021.

Shen, C., Shen, A., Cui, Y., Chen, X., Liu, Y., Fan, Q., Chan, P., Tian, C., Wang, C., and Lan, J.: Spatializing the roughness length of heterogeneous urban underlying surfaces to improve the WRF simulation-part 1: A review of morphological methods and model evaluation, Atmos. Environ., 270, 118874, https://doi.org/10.1016/j.atmosenv.2021.118874, 2022.

Shen, Y., Liu, J., Chen, Z., Yang, M., Shu, L., Gai, C., and Jiang, Y.: Influence of wind flows on surface O_3 variation over a Coastal Province in Southeast China, Atmosphere, 15, 262, https://doi.org/10.3390/atmos15030262, 2024.

Siewert, J. and Kroszczynski, K.: Evaluation of high-resolution land cover geographical data for the WRF model simulations, Remote Sens., 15, 2389, https://doi.org/10.3390/rs15092389, 2023.

Solazzo, E., Bianconi, R., Vautard, R., Appel, K. W., Moran, M. D., Hogrefe, C., Bessagnet, B., Brandt, J., Christensen, J. H., Chemel, C., Coll, I., Denier van der Gon, H., Ferreira, J., Forkel, R., Francis, X. V., Grell, G., Grossi, P., Hansen, A. B., Jeričević, A., Kraljević, L., Miranda, A. I., Nopmongcol, U., Pirovano, G., Prank, M., Riccio, A., Sartelet, K. N., Schaap, M., Silver, J. D., Sokhi, R. S., Vira, J., Werhahn, J., Wolke, R., Yarwood, G., Zhang, J., Rao, S. T., and Galmarini, S.: Model evaluation and ensemble modelling of surface-level ozone in Europe and North America in the context of AQMEII, Atmos. Environ., 53, 60–74, https://doi.org/10.1016/j.atmosenv.2012.01.003, 2012.

Tarasick, D., Galbally, I. E., Cooper, O. R., Schultz, M. G., Ancellet, G., Leblanc, T., Wallington, T. J., Ziemke, J., Liu, X., and Steinbacher, M.: Tropospheric Ozone Assessment Report: Tropospheric ozone from 1877 to 2016, observed levels, trends and uncertainties, Elem. Sci. Anth., 7, 39, https://doi.org/10.1525/elementa.376, 2019.

Wang, K., Tong, Y., Gao, J., Gao, C., Wu, K., Yue, T., Qin, S., and Wang, C.: Impacts of LULC, FDDA, Topo-wind and UCM schemes on WRF-CMAQ over the Beijing-Tianjin-Hebei region, China, Atmos. Pollut. Res., 12, 292–304, 2021a.

Wang, N., Lyu, X., Deng, X., Huang, X., Jiang, F., and Ding, A.: Aggravating O_3 pollution due to NO_x emission control in eastern China, Sci. Total Environ., 677, 732–744, 2019.

Wang, N., Xu, J., Pei, C., Tang, R., Zhou, D., Chen, Y., Li, M., Deng, X., Deng, T., and Huang, X.: Air quality during COVID-19 lockdown in the Yangtze River Delta and the Pearl River Delta: Two different responsive mechanisms to emission reductions in China, Environ. Sci. Technol., 55, 5721–5730, 2021b.

Wang, N., Huang, X., Xu, J., Wang, T., Tan, Z.-M., and Ding, A.: Typhoon-boosted biogenic emission aggravates cross-regional ozone pollution in China, Sci. Adv., 8, eabl6166, https://doi.org/10.1126/sciadv.abl6166, 2022.

Wang, N., Du, Y., Chen, D., Meng, H., Chen, X., Zhou, L., Shi, G., Zhan, Y., Feng, M., Li, W., Chen, M., Li, Z., and Yang, F.: Spatial disparities of ozone pollution in the Sichuan Basin spurred by extreme, hot weather, Atmos. Chem. Phys., 24, 3029–3042, https://doi.org/10.5194/acp-24-3029-2024, 2024.

Wang, T., Xue, L., Brimblecombe, P., Lam, Y. F., Li, L., and Zhang, L.: Ozone pollution in China: A review of concentrations, meteorological influences, chemical precursors, and effects, Sci. Total Environ., 575, 1582–1596, 2017.

Wang, Y., Logan, J. A., and Jacob, D. J.: Global simulation of tropospheric O_3-NO_x-hydrocarbon chemistry: 2. Model evaluation

and global ozone budget, J. Geophys. Res.-Atmos., 103, 10727–10755, 1998.

Wang, Y., Gao, W., Wang, S., Song, T., Gong, Z., Ji, D., Wang, L., Liu, Z., Tang, G., and Huo, Y.: Contrasting trends of PM2.5 and surface-ozone concentrations in China from 2013 to 2017, Nat. Sci. Rev., 7, 1331–1339, 2020.

WHO: Ambient air pollution: a global assessment of exposure and burden of disease, World Health Organization, Geneva, Switzerland, ISBN 9789241511353, 2016.

Willmott, C. J.: On the validation of models, Phys. Geogr., 2, 184–194, 1981.

Yahya, K., He, J., and Zhang, Y.: Multiyear applications of WRF/Chem over continental US: Model evaluation, variation trend, and impacts of boundary conditions, J. Geophys. Res.-Atmos., 120, 12748–12777, 2015.

Yarwood, G., Jung, J., Whitten, G. Z., Heo, G., Mellberg, J., and Estes, M.: Updates to the Carbon Bond mechanism for version 6 (CB6), 9th Annual CMAS Conference, Chapel Hill, NC, 11–13, https://www.cmascenter.org/conference/2010/abstracts/emery_updates_carbon_2010.pdf (last access: 9 May 2026), 2010.

Zhang, J., Wei, Y., and Fang, Z.: Ozone pollution: a major health hazard worldwide, Front. Immunol., 10, 2518, https://doi.org/10.3389/fimmu.2019.02518, 2019a.

Zhang, Q., Zheng, Y., Tong, D., Shao, M., Wang, S., Zhang, Y., Xu, X., Wang, J., He, H., and Liu, W.: Drivers of improved PM2.5 air quality in China from 2013 to 2017, P. Natl. Acad. Sci. USA, 116, 24463–24469, 2019b.

Zhao, F., Liu, C., Hu, Q., Xia, C., Zhang, C., and Su, W.: High Spatial Resolution Ozone Profiles Retrieved from the First Chinese Ultraviolet–Visible Hyperspectral Satellite Instrument, Engineering, 32, 106–115, 2024.

Zheng, B., Cheng, J., Geng, G., Wang, X., Li, M., Shi, Q., Qi, J., Lei, Y., Zhang, Q., and He, K.: Mapping anthropogenic emissions in China at 1 km spatial resolution and its application in air quality modeling, Sci. Bull., 66, 612–620, 2021.

Zhu, Q., Bi, J., Liu, X., Li, S., Wang, W., Zhao, Y., and Liu, Y.: Satellite-based long-term spatiotemporal patterns of surface ozone concentrations in China: 2005–2019, Environ. Health Persp., 130, 027004, https://doi.org/10.1289/ehp9406, 2022.

Zhu, Y., Liu, Y., Li, S., Wang, H., Lu, X., Wang, H., Shen, C., Chen, X., Chan, P., Shen, A., Wang, H., Jin, Y., Xu, Y., Fan, S., and Fan, Q.: Assessment of tropospheric ozone simulations in a regional chemical transport model using GEOS-Chem outputs as chemical boundary conditions, Sci. Total Environ., 906, 167485, https://doi.org/10.1016/j.scitotenv.2023.167485, 2024.